Research Article Vol. 13, No. 12 / December 2026 / Optica 2459



Complex-field meta-microscopy with high spatial and phase-gradient resolution

Qi Liu,[1] Wenwei Liu,[1,5] Qiang Li,[2] Duk-Yong Choi,[3] Zhancheng Li,[1] Yongliang Liu,[1] Bo Yu,[1] Yifei Xu,[1] Hua Cheng,[1,6] and Shuqi Chen[1,2,4,7]

[1]The Key Laboratory of Weak Light Nonlinear Photonics, Ministry of Education, School of Physics and TEDA Institute of Applied Physics, Nankai University, Tianjin 300071, China
[2]School of Materials Science and Engineering, Nankai University, Tianjin 300350, China
[3]Laser Physics Centre, Research School of Physics, Australian National University, Canberra, ACT 2601, Australia
[4]The Collaborative Innovation Center of Extreme Optics, Shanxi University, Taiyuan, Shanxi 030006, China
[5]wliu@nankai.edu.cn
[6]hcheng@nankai.edu.cn
[7]schen@nankai.edu.cn

Received 30 July 2026; revised 23 September 2026; accepted 24 October 2026; published 17 November 2026

The pursuit of obtaining richer parallel information about optical fields has long been a central and enduring theme in optical imaging technology. Conventional imaging systems struggle to jointly image the complex amplitude of an object or a wavefront, and this limitation becomes particularly severe in scenarios requiring high resolution, such as label-free biological detection, material diagnosis, and optical quantitative characterization. Here, we theoretically propose and experimentally demonstrate a complex-field meta-microscopy based on a focusing-interferometry multiplexing strategy enabling both high spatial (including intensity and phase imaging) and phase-gradient resolution. A spatial-light-modulator-generated phase gradient of 7.5×10^{-4} rad/μm is experimentally reconstructed, and the spatial resolution of phase images is improved by four times using a physics-based self-supervised super-resolution neural network framework, leading to simultaneously enhanced joint resolution of complex-amplitude and phase gradient. We also realize the two-dimensional monitoring of the ultraviolet-induced refractive-index distribution in photoresist based on the proposed meta-microscopy, with an index resolution reaching $\sim 4 \times 10^{-5}$. The proposed scheme opens up possibilities for compact and exceptional complex-amplitude imaging with high fidelity, and holds potential for applications such as subcellular biological detection, material denaturation characterization, and nondestructive evaluation. © 2026 Optica Publishing Group under the terms of the Optica Open Access Publishing Agreement

https://doi.org/10.1364/OPTICA.612791

1. INTRODUCTION

Optical imaging has long been serving as a cornerstone of optics and photonics, enabling visualization of phenomena across scales—from cellular structures to cosmic events [1]. Central to its evolution is the pursuit of richer information content: not merely intensity, but also phase, polarization, and spectral signatures [2–4]. Intensity imaging is one of the most fundamental techniques providing essential information about the geometric morphology and brightness profile of the target object. Phase imaging, which can hardly be directly detected by conventional photodetectors, provides access to refractive index variations, surface topography, and wavefront distortions—parameters essential for applications ranging from biomedical diagnostics [5,6], computational optics [7,8], holography [9,10], and wavefront sensing to precision metrology.

In the past decades, researchers have developed various strategies to obtain phase information with interference or non-interference methods. The interference methods can convert phase information to intensity contrast by interference of the wavefront, such as phase-contrast imaging and holography [11,12]. To reduce the complexity of the interferometric setup and broaden the applicable scenarios, non-interference methods such as Shack–Hartmann sensing [13] have been proposed to retrieve the wavefront to be detected. However, conventional complex-amplitude imaging systems suffer from a trade-off in resolution when jointly acquiring intensity, phase, and phase-gradient images. Generally, besides the intensity channel, the acquisition of phase and phase-gradient images also requires mapping the phase-contrast information onto the intensity distribution due to the absence of a direct phase-type photodetector. As a result, these imaging channels share the limited space-bandwidth product, which characterizes the information-carrying capacity of an optical system [14]. To separate these imaging channels without aliasing, the space-bandwidth product must be allocated between different information channels, which compromises the achievable resolutions in different imaging channels for a given field of view (FOV). Quadriwave lateral shearing interferometry (QLSI) is a well-established framework to realize resolution-limited quantitative

phase imaging [15,16]. However, conventional cross-grating-based QLSI implementations face inherent physical bottlenecks to suppress parasitic diffraction orders, and the grating period restricts spatial sampling density and phase resolution. Other representative phase-retrieval strategies present distinct operational challenges: Fourier ptychographic imaging (FPI) [17,18] combines intensity and phase imaging in a single physical process, whereas multi-shot acquisition is required to stitch the spatial frequency spectrum. Solving the transport of intensity equation (TIE) [19,20] may provide another solution, but it is limited to the paraxial approximation and the weak phase object approximation. In recent years, deep learning has offered a data-driven approach to phase reconstruction by leveraging prior knowledge; however, its advancement is hampered by the data-intensive pre-training, limited generality, and insufficient recovery of high-frequency details [21,22].

Recent advances in flat optics and nanophotonics have ushered in a new paradigm for compact and multifunctional wavefront control using metasurfaces [23–25]. These planar arrays of subwavelength resonators can realize local and nonlocal electromagnetic (EM) resonances, thereby manipulating optical amplitude [26,27], phase [28,29], and polarization [30,31] with unprecedented precision compared with traditional optical components. Metasurface-enabled imaging systems have presented remarkable capabilities in beam shaping [32,33], aberration correction [34,35], FOV expansion [36], and spectral imaging [37,38]. To recover the wavefront of EM waves, metalens arrays have been proposed to realize Shack–Hartmann sensing [39]. By performing multi-focal imaging and solving the TIE, a focus-tunable metalens can also recover the wavefront for quantitative phase retrieval [40]. Besides, polarization-modulated diffractive optical elements enable single-shot phase measurement by encoding phase information into polarization-dependent diffraction patterns [41]. Recently, researchers have developed a metalens to realize complex amplitude imaging using shearing interference and incoherent summation of two orthogonally polarized channels, which opens up a new possibility for compact and versatile detection in surface metrology and biological characterization [42]. For complex-amplitude imaging, spatial resolution and phase gradient sensitivity are both important metrics, reflecting the capability to resolve fine structural details and weak wavefront slopes, respectively. However, due to the limited space-bandwidth product, diffraction efficiency, and signal-to-noise ratio (SNR), achieving high-resolution (HR) complex-field imaging simultaneously in the spatial and phase-gradient dimensions remains challenging, particularly for two-dimensional imaging.

Here, taking advantage of metasurfaces with local EM manipulation of polarization and phase, we propose a meta-microscopy enabling HR two-dimensional complex-amplitude imaging. By combining intensity imaging and lateral shear interferometry into a single pluggable metalens, we extract the intensity and phase distribution of the incident wavefront. We also employ a self-supervised neural network to co-register and align the intensity and phase, further enabling enhanced imaging of transparent label-free cells. We demonstrate real-time and sensitive monitoring of the refractive-index distribution in a photoresist film under ultraviolet (UV) exposure. We expect that the proposed HR complex-amplitude meta-microscopy can unlock possibilities for compact high-performance imaging ranging from biological detection and material diagnosis to micro–nano manufacturing.

2. RESULTS

A. Principle and Design Strategy of HR, High-Sensitivity Complex-Amplitude Imaging Metasurfaces

For incident light carrying complex-amplitude information $A_0(x, y)e^{i\varphi_0(x,y)}$, we aim to separate and retrieve the intensity $A_0(x, y)$ and phase $\varphi_0(x, y)$ through polarization multiplexing in the x- and y-polarization channels, as illustrated in Fig. 1(a). The intensity image provides high-spatial-resolution amplitude information limited by the Rayleigh diffraction criterion, while phase reconstructions derived from the interferograms via specialized reconstruction algorithms yield high-sensitivity phase gradient data at a lower spatial resolution. Leveraging these complementary inputs, HR intensity images, and low-resolution (LR) phase images, we employ a self-supervised deep neural network (physics-based guided phase super-resolution, PGSR) to jointly enhance the spatial resolution of both modalities, as shown in Fig. 1(b).

In the x-polarization channel, the metasurface acts as a metalens, governed by the phase distribution $\Phi_x(x, y) = -k_0(\sqrt{x^2 + y^2 + f^2} - f)$ as indicated in the upper panel of Fig. 1(c), where λ is the operating wavelength and f denotes the focal length. In the y-polarization channel, as schematically illustrated in the bottom panel of Fig. 1(c), a 2×2 array of unit cells is treated as a single supercell during the design process. Within the momentum space, the supercell introduces four distinct momentum components possessing an identical magnitude $|k_{\text{shear}}| = 2\pi/\lambda \sin\theta$. In real space, the four constituent unit cells (denoted as i, ii, iii, and iv) within each supercell collectively generate four phase gradients along four directions with $\alpha_j = 45°$, $-45°$, $135°$, and $-135°$, respectively, and the phase profile can be correspondingly represented as $\Phi_y^{(j)}(x, y) = k_{shear}(x \cos\alpha_j + y \sin\alpha_j)$. Our design also carefully balances several physical constraints. Increasing the shearing angle reduces the interference period and enhances measurement sensitivity; however, as dictated by the grating equation, exceeding a certain angle threshold introduces unwanted higher-order diffractions that drain optical power. Conversely, decreasing the shearing angle enlarges the interference period, which reduces the spatial sampling density of the fringes. Furthermore, while reducing the metasurface lattice period can support larger shearing angles, it intensifies near-field coupling between adjacent structures, causing the actual transmitted field to deviate from the ideal phase profile and generating additional parasitic orders. The simulated diffraction efficiency for a $100 \times 100\ \mu m^2$ metasurface is 48% normalized by the total transmission. Considering the minimum working distance of 100 μm, the effective efficiency calculated within the detection area used for interferogram reconstruction reaches 78%, as most residual background signals are spatially separated from this region. The resulting phase distribution across these units is combined in Fig. 1(b) (top panel), leading to lateral shear interference before spatially divergent propagation. The fabricated metasurface is visualized via optical and scanning electron microscopy (SEM) in Figs. 1(d) and 1(e).

The metasurface consists of hydrogenated amorphous silicon (a-Si:H) nanopillars with a high refractive index and low intrinsic loss on a fused silica substrate at an operating wavelength of 750 nm. The size of the unit cell is set to be 350 nm, and the supercell for y-polarization extends to 700 nm while suppressing high-order diffraction. Each nanopillar resonator with height

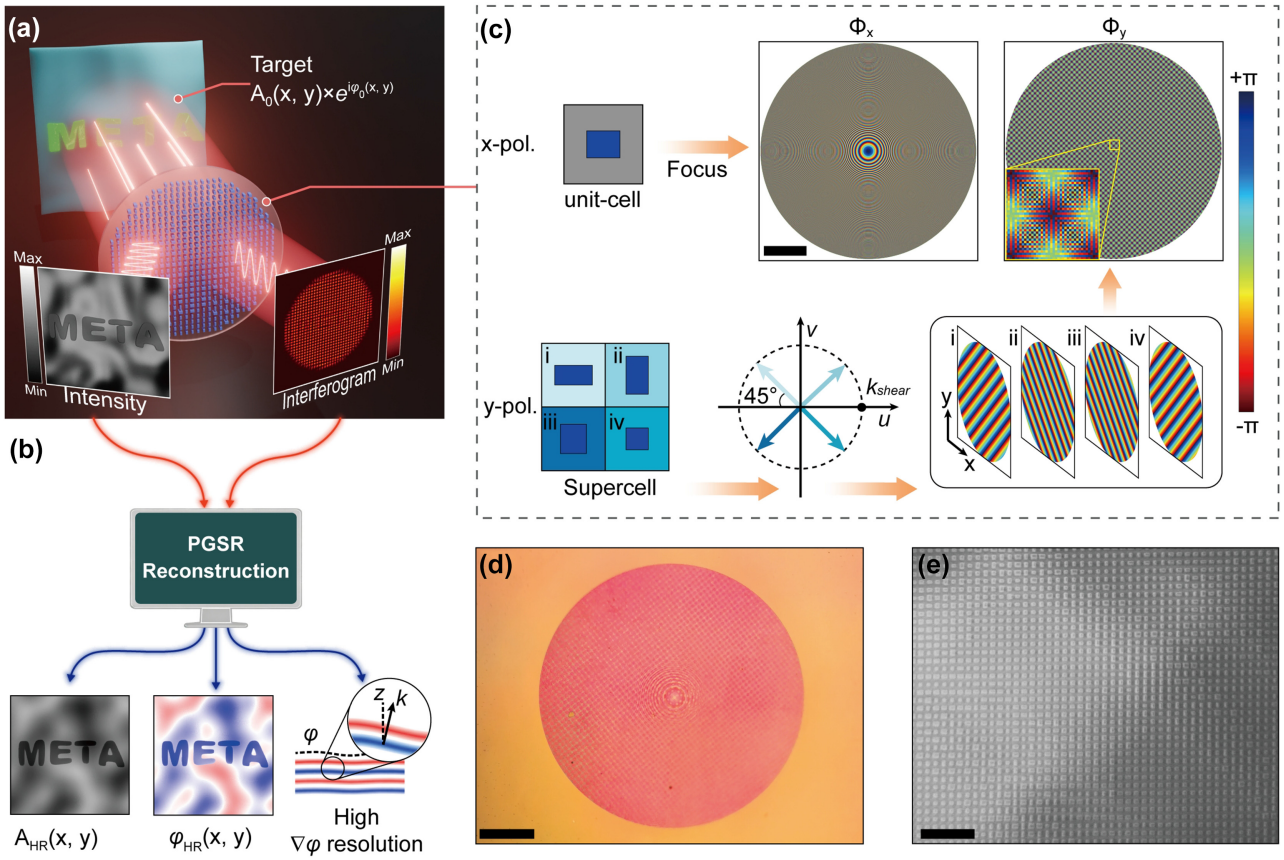


Fig. 1. Schematic of the design principle of meta-microscopy. (a) The complex-amplitude information of the object is modulated by the metasurface, undergoing imaging and shearing interference in the x- and y-polarization channels, respectively. (b) Reconstruction of HR complex amplitude. The intensity image and interferogram are processed to recover HR complex amplitude and highly sensitive phase-gradient information. (c) The unit cell in the x-polarization channel is arranged for metalens imaging (top). The supercell design in the y-polarization channel and the corresponding lateral momentum components leading to shear interferometry (bottom). Scale bar: 100 μm. (d) Optical microscopy image of the fabricated metasurface, scale bar: 100 μm. (e) SEM image of the fabricated metasurface, scale bar: 5 μm.

$H = 500$ nm modulates the propagation phase by varying its in-plane dimensions L_x and L_y. As summarized in Figs. 2(a) and 2(b), full-wave EM simulations map the phase shift and transmittance across a parametric space $\{L_x, L_y\}$, establishing a response library to match the required target phase profiles $\Phi_x(x, y)$ and $\Phi_y(x, y)$. Simulated and experimental intensity profiles at the focal plane ($z = 300$ μm) are compared in Figs. 2(d) and 2(e). The numerical aperture (NA) of the metalens is set to 0.6 under x-polarization. The supercell design generates shear interference under y-polarization [Fig. 2(f)]. Compared with the simulated interference pattern [Fig. 2(g)], the measured interference pattern [Fig. 2(h)] exhibits consistent fringe spacing and contrast. To minimize the central spot in the interference pattern, which is attributed to the coupling with the x-polarization channel owing to the overlap between two phase distributions, we performed a feedback-based optimization by incorporating distinct weighting factors and constraints on both the intensity and phase profiles under x- and y-polarization (see Supplement 1, Section S2). The residual tiny central real-space spot in the experimental interference pattern is due to fabrication imperfections. To quantify the effects of the crosstalk and noise in the optical system, we calculated reconstruction fidelity under various crosstalk levels and SNRs. In our experiments, the crosstalk level ranges from −24 to −27 dB [extracted from Figs. 2(e) and 2(h)] and the typical SNR is 40 dB (Supplement 1, Section S2), which yields a relative root-mean-square error (RMSE) for phase reconstruction of around 3% of the peak-to-valley (PV) value. For intensity imaging, the crosstalk is also acceptable based on the calculated peak signal-to-noise ratio (PSNR) and structural similarity index measure (SSIM) [43] (see details in Supplement 1, Section S2).

When incident light with complex amplitude $A(x, y)e^{i\varphi(x,y)}$ passes through the metasurface and undergoes shearing interference with a shear distance Δd, the resulting electric field intensity distribution is described by

$$I(x, y) = I_0(x, y)\left[1 + \sum_{i=1}^{4} a_i \cos\left(b_i \frac{\partial\varphi}{\partial \mathbf{n}_i} + 2k_{\text{shear}}\mathbf{n}_i\right)\right], \tag{1}$$

where $I_0(x, y) = |A(x, y)|^2$ is the intensity distribution of the incident light; $\mathbf{n}_i$ represents the direction of shear interference labeled by $i = 1, 2, 3, 4$; $\partial\varphi/\partial \mathrm{n}_i$ is the phase gradient along each direction; a_i is the relative contribution of each directional shearing term ($a_1 = a_2 = 1/2$, $a_3 = a_4 = 1/4$); b_i is the shear distance ($b_1 = b_2 = \Delta d$, $b_3 = b_4 = \sqrt{2}\Delta d$). Equation (1) implies that the phase term of the complex amplitude becomes encoded in the interference pattern after being modulated by the metasurface. Consequently, the phase gradient information is manifested in

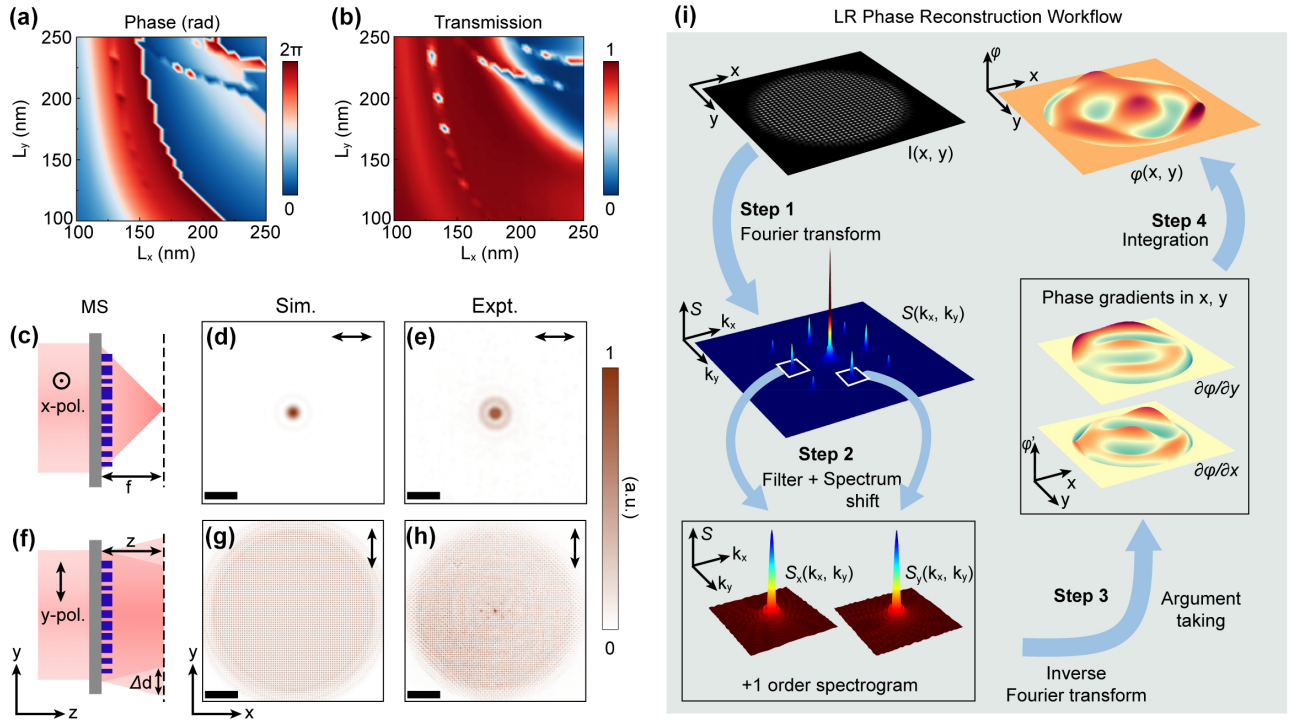


Fig. 2. Metasurface characteristics and the workflow of the LR phase reconstruction algorithm. (a), (b) Simulated phase (a) and transmittance (b) distributions of the unit cell for various nanopillar widths L_x and L_y. (c) Schematic of the metasurface for focusing. (d), (e) the simulated (d) and experimental (e) focusing spot profiles at the focal plane. (f) Schematic of the metasurface for shear interference. (g), (h) The simulated (g) and experimental (h) interferograms at a propagation distance z. (i) The flowchart for LR phase reconstruction of the incident wavefront from the captured interferogram.

the intensity image, enabling phase recovery from a single interferogram, as shown in Fig. 2(i). To compensate the deformation of wavefronts introduced in experiments such as tilt, offset, and other anomalies, a calibration process is employed (see Fig. S10 in Supplement 1, Section S6). The calibrated interferogram $I(x, y)$ is transformed into the spatial frequency domain $S(k_x, k_y)$ via a Fourier transform (FT):

$$S(k_x, k_y) = \mathcal{F}[I(x, y)] = S_0(k_x, k_y) + \sum_{i=1}^{4} \frac{a_i}{2} \left[S_i(k_x, k_y) \otimes \delta(k_x - 2k_{\text{shear}} l_i, k_y - 2k_{\text{shear}} m_i) + S_i(k_x, k_y) \otimes \delta(k_x + 2k_{\text{shear}} l_i, k_y + 2k_{\text{shear}} m_i) \right], \quad (2)$$

where $S_0(k_x, k_y)$ is the FT of $I_0(x, y)$, S_i is the FT of $I_0(x, y) \exp(i b_i \partial\varphi/\partial \mathbf{n}_i)$, $\otimes$ denotes the convolution operation, δ is the Dirac delta function, and (l_i, m_i) for $i = 1, 2, 3, 4$ are $(1, 0)$, $(0, 1)$, $(1, 1)$, and $(1, -1)$, respectively. $S(k_x, k_y)$ contains a central zeroth-order peak and distinct $\pm$1st-order peaks corresponding to the designed lateral momenta along 0°, ±45°, and 90°. The phase gradient information of the incident wavefront is encoded within these $\pm$1st-order peaks according to Eq. (2). Subsequently, a high-pass spectral filter is applied to isolate the +1st-order spectra along the x and y directions (the −1st-order is the same owing to parity symmetry). Frequency shifting is then performed to center the spectral peaks at the origin, yielding $S_x(k_x, k_y)$ and $S_y(k_x, k_y)$ as illustrated in Step 2 of Fig. 2(i). Next, the inverse FT is applied to the centered spectra to obtain the phase gradient, expressed as $\arg\{\mathcal{F}^{-1}[S_i(k_x, k_y)]\}$. The phase gradient components $\partial\varphi/\partial x$ and $\partial\varphi/\partial y$ are then derived using a phase-unwrapping algorithm based on reliability sorting along a discontinuous path [44]. Finally, the reconstructed phase is calculated from the acquired phase gradient using the gradient integration algorithm (see details in Supplement 1, Section S1).

B. High-Accuracy Phase Gradient Reconstruction and Imaging

To quantify the performance of phase reconstruction, we employed a reflective phase-type spatial light modulator (SLM) to generate the predefined phase distributions. In our experimental setup, the SLM was optically demagnified by a factor of 5 using a beam-shrinking 4f system composed of 150 and 30 mm lenses. The modulated light then passed through the metasurface, and the resulting interferograms were collected by a 20× objective (Sigma PAL-20-HR, NA = 0.6) and captured by an sCMOS camera (Hamamatsu C13440-20CU). For different PV amplitudes [2π, 0.2π in Figs. 3(a) and 3(b)] of the phase patterns with identical wavefront profiles, the metasurface can reconstruct the predefined wavefronts. Fourier-domain compensation is further used to remove background wavefront aberrations from the experimental setup; it does not improve the optical resolution, but is required for accurate phase extraction (Supplement 1, Section S4). The RMSE between the reconstructed and SLM-loaded phases was consistently measured to be within 5% of the PV amplitude for all conditions. Additional comparative results are provided in Supplement 1, Section S8.

To experimentally evaluate the phase-gradient reconstruction capability, we programmed the minimum available phase gradient of the SLM, g_{SLM}, which is determined by

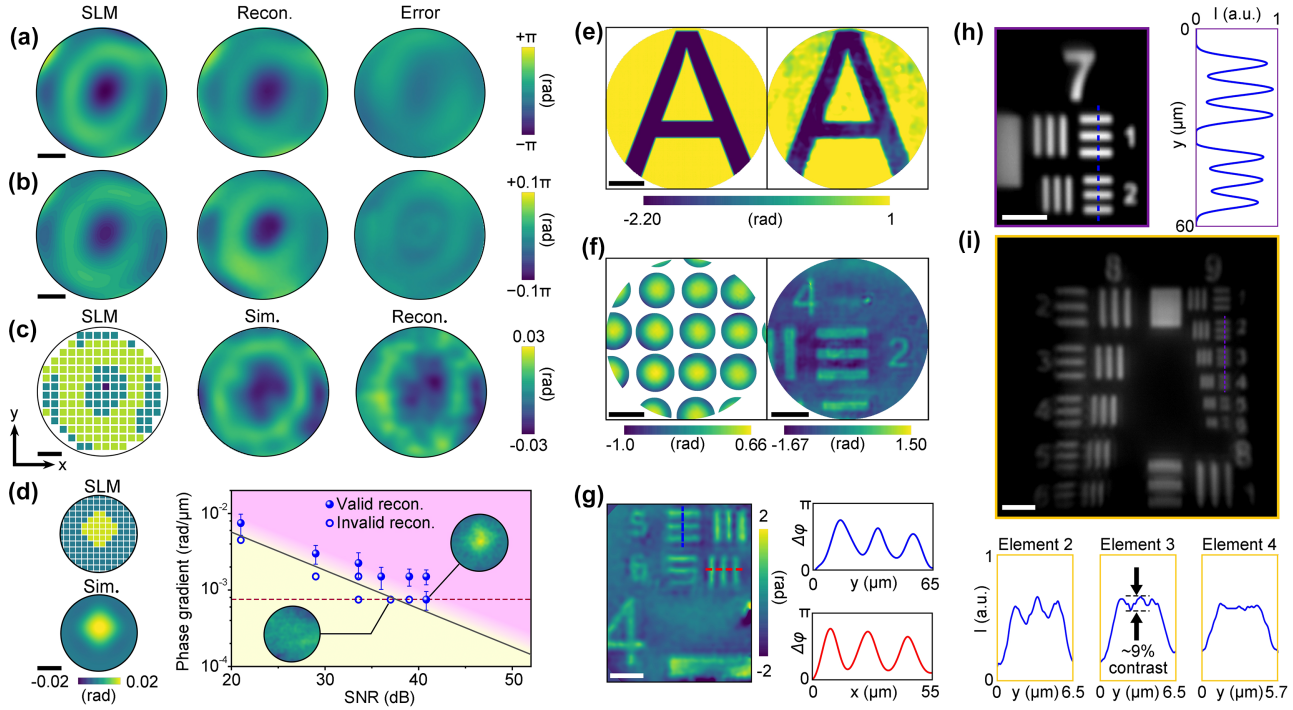


Fig. 3. Experimental validation of quantitative phase reconstruction and HR intensity imaging. (a), (b) Quantitative phase reconstruction of identical spatial profiles with varying PV values of 2π (a) and 0.2π (b). Each panel displays (from left to right) the ground-truth phase loaded on the spatial light modulator (SLM), the experimentally reconstructed phase, and the absolute error. (c) Evaluation of phase gradient sensitivity. Panels show (from left to right) the minimum phase gradient loadable on the SLM, the simulated wavefront, and the experimentally reconstructed phase. (d) Experimental evaluation of the SNR-dependent phase-gradient resolution. Left: phase pattern loaded on the SLM and the corresponding simulated phase distribution after propagation. Right: phase-gradient as a function of the measured overall SNR. Filled and open circles denote valid and invalid reconstructions. The red dashed and black lines indicate g_{SLM} and theoretical minimum phase-gradient, respectively. Insets: reconstructed phase patterns. (e) Ground-truth patterned phase (letter "A") loaded on the SLM (left) and the corresponding experimental reconstruction (right). (f) Experimental phase reconstruction of a commercial microlens array (left) and a phase-type USAF 1951 resolution target (right). (g) Spatial resolution of phase reconstruction measured using a phase-type USAF 1951 resolution target, with cross-sectional phase profiles extracted along the blue and red dashed lines (resolving Group 5, Element 6). (h) Intensity image of a standard amplitude-type USAF 1951 target (Group 7) and the corresponding cross-sectional profile along the blue dashed line. (i) Intensity image resolving the finest features of the target (Groups 8 and 9), with the cross-sectional profile for Group 9, Elements 2–4 shown at the bottom. Scale bars: 100 μm in (a), (b), (e), and (f); 25 μm in (c); 28 μm in (d); 50 μm in (g); 20 μm in (h); 10 μm in (i).

the SLM phase step, pixel size, and system magnification. For our 8-bit SLM, the minimum attainable phase step is $\Delta\varphi = 2\pi/256 \approx 0.0245$ rad, leading to a minimized phase gradient of $\Delta\varphi/p$, where p is the pixel size of the SLM. To obtain a finer phase gradient, we used a single lens with a magnification $M_y = 5$ to reduce the attainable phase gradient to $g_{\mathrm{SLM}} = \Delta\varphi/(p \times M_y) \approx 7.5 \times 10^{-4}$ rad/μm (see Supplement 1, Section S7). Furthermore, to reduce the higher phase gradient generated by the discontinuity of SLM pixels, we employed an iris to perform spatial filtering (see Fig. S11, Supplement 1), which enables the generation and measurement of phase profiles with gradients below the SLM's native minimum. As shown in Fig. 3(c), the SLM phase pattern contains three phase levels $\{-\Delta\varphi, 0, \Delta\varphi\}$, leading to a PV value of $2\Delta\varphi$, and the phase gradients fall within the range $[-7.5 \times 10^{-4}, 7.5 \times 10^{-4}]$ rad/μm. The experimentally reconstructed profile agrees with the simulated phase distribution, showing that the programmed gradient $g_{\mathrm{SLM}} = 7.5 \times 10^{-4}$ rad/μm can be reconstructed at a detection distance of 100 μm, with an RMSE of 1.6×10^{-4} rad/μm. The measured absolute phase sensitivity is 0.049 rad with an absolute RMSE of 0.0084 rad, which is limited by the minimum phase step of the 8-bit SLM used in our experiments.

As discussed in Supplement 1, Section S2, the minimum phase gradient g_{lim} the system can resolve depends on the experimental SNR. We performed measurements at controlled SNR levels while keeping the other optical setup the same. The SNR of the system can be changed by varying the camera exposure time from 50 to 200 ms with an interval of 25 ms (to obtain a higher SNR, we used a Goldeye G-130 VSWIR TEC1 in this characterization). To extract the specific value of SNR from the captured interferograms, we captured eight raw interferograms for each exposure time and evaluated the intensity variance at each pixel (details in Supplement 1, Section S2). As shown in Fig. 3(d), the measured minimum resolvable phase gradient improves as the SNR increases. The reconstruction was classified as failed when the normalized RMSE (NRMSE) of the phase gradient was greater than 1. Note that the SNR includes fluctuations from both the CMOS and the optical setup. In our measurement, the SNR of the CMOS is 51.5 dB, and the overall SNR can be further enhanced by suppressing environmental noise.

In addition to these smooth and weak-gradient phase profiles, we further tested a patterned phase distribution in the form of the letter "A" loaded onto the SLM. As shown in Fig. 3(e), the reconstructed phase image preserves the overall geometry and sharp boundaries of the programmed pattern, confirming the capability

of the metasurface to recover complex spatial phase distributions. We also experimentally reconstructed the phase distributions of a commercial microlens array (Thorlabs MLA150-7AR-M) and a fabricated phase-type United States Air Force (USAF) 1951 resolution target, as shown in Fig. 3(f). The microlens array provides a continuous and smoothly varying phase profile, whereas the phase-type USAF target provides sharp phase discontinuities and high-spatial-frequency features.

The spatial phase resolution characterizes the system's ability to resolve fine morphological phase features. This metric is fundamentally governed by the interference fringe period in experiments and the filtering in the algorithm. To quantify the spatial resolution of phase, we used the phase-only USAF 1951 resolution target in SU-8 photoresist with an etched π phase step. As shown in Fig. 3(g), under y-polarization without super-resolution, our system resolves features down to Group 5, Element 6, corresponding to a minimum resolvable line width of 8.77 μm (57 lp/mm). Note that this spatial resolution is slightly coarser than the fundamental interference fringe period (6.08 μm). That is because during phase reconstruction, a finite spectral filtering operation is required in the Fourier domain to isolate the first-order spectrum and suppress zero-order cross-talk, which imposes a low-pass filtering effect on the ultimate spatial resolution.

Note that Eq. (1) relies on the first-order Taylor expansion of the phase difference between the sheared wavefronts. When steep phase gradients exist in the optical system, higher-order Taylor components become non-negligible and introduce systematic errors, including spatial frequency shift and spectral aliasing. To guarantee the validity of Eq. (1) without spectral aliasing, the maximum detectable phase gradient for our system is 0.17 rad/μm, considering the lateral shear period of 6.08 μm and the detection distance of 300 μm (the maximum phase gradient reaches 0.51 rad/μm when decreasing the detection distance to 100 μm). Such a limit can lead to blurred edges and a loss of high-spatial-frequency phase information for fine biological features. For applications requiring larger detectable phase gradients, two optical strategies can be employed. First, a microscopic magnification system can be integrated before the metasurface to optically enlarge the object to be imaged, ensuring that its fine structures exceed the interference period. Second, the metasurface can be designed to produce a larger shearing angle; this would correspondingly reduce the interference period, directly enhancing the system's ability to sample high-frequency phase variations. Under such strategies, we can enhance the maximum phase-gradient magnitude and simultaneously leverage the HR capability of our technique for imaging.

To validate the spatial intensity resolution, characterization was conducted using a standard amplitude-type USAF 1951 resolution test chart. For intensity measurement, two objective lenses were arranged in a conjugate configuration to project a 1:1 real image of the target onto the metasurface. The transmitted intensity distribution was then collected by the 20× objective and captured by the sCMOS camera. Figures 3(h) and 3(i) show the HR imaging results in the x-polarized channel and the corresponding cross-sectional profiles. The system clearly resolves the features of Group 7 [Fig. 3(h)] and the finest structures in Groups 8 and 9 [Fig. 3(i)]. Based on the cross-sectional profile of Group 9, Elements 2–4, the spatial intensity resolution achieves a smallest resolvable feature of ~ 0.78 μm (Group 9, Element 3, 9% fringe visibility), which closely approaches the theoretical diffraction limit of our optical system (0.71 μm). For the x-polarized intensity channel, we employ an aperture stop in the experimental setup to filter out aberrated edge regions to ensure consistent image quality, leading to an FOV of 200×200 μm^2. For the y-polarization phase channel, imaging is based on free-space interference fringe formation rather than focusing. Consequently, the usable FOV can be characterized by the physical aperture of the metasurface subtracting the shear distance, yielding 484 μm in diameter. Within this region, the interference contrast remains sufficiently uniform for reliable phase retrieval.

C. HR Complex-Amplitude Imaging

The combination of intensity and phase enables the reconstruction of the object's complex amplitude distribution. However, although the phase channel is highly sensitive, it is still limited in spatial resolution by the period of the interference fringes. Based on the principle of phase reconstruction, the spatial resolution of the reconstructed phase is coarser than the period of the interference fringes, since the maximum spatial frequency of the reconstructed phase must be lower than that of the interference fringes. In contrast, the intensity image exhibits a higher spatial resolution.

To harmonize the spatial resolutions of the two channels, we developed a physics-based guided phase super-resolution (PGSR) framework. The goal of PGSR is not to infer the phase solely from intensity. Rather, it combines the quantitative low-spatial-frequency phase information measured by y-polarization with the HR structural information provided by x-polarization. As illustrated in Fig. 4(a), the HR intensity image I_{HR} and the LR phase measurement φ_{LR} are used as the two inputs to PGSR-Net. The intensity branch extracts structural features from I_{HR}, while the phase branch extracts phase features from φ_{LR} and upsamples them to the HR size. The two feature streams are fused through a local structure-phase modulation module, allowing local structural cues in the intensity image to guide the recovery of missing phase details. The reconstruction head predicts a residual phase component $\Delta\varphi$, and the final HR phase estimate is obtained as $\varphi'_{\mathrm{HR}} = \mathrm{Up}(\varphi_{\mathrm{LR}}) + \Delta\varphi$, where $\mathrm{Up}(\cdot)$ denotes upsampling. This residual formulation anchors the reconstruction to the measured phase channel. The low-frequency phase content and absolute phase scale are inherited from φ_{LR}, while the network mainly recovers the missing high-spatial-frequency phase components guided by the HR intensity image. A key element of PGSR is the use of a physical consistency constraint for self-supervised training. The measured LR phase in our system is not produced by a conventional digital degradation process, such as bicubic down-sampling or Gaussian blurring. It is generated by shear-interferometric acquisition, followed by Fourier-domain phase reconstruction. We therefore model the dominant resolution-limiting steps of this process, including diagonal shear displacement and spatial-frequency filtering, using a differentiable physical forward model $H(\cdot)$. During training, the predicted HR phase is mapped back to the LR measurement domain as $\varphi'_{\mathrm{LR}} = H(\varphi'_{\mathrm{HR}})$. The physical consistency is then computed as the L_1 difference between the simulated and measured LR phase maps, $L_{\mathrm{phys}} = \|\varphi'_{\mathrm{LR}} - \varphi_{\mathrm{LR}}\|_1$. This term provides the primary measurement constraint and ensures that the supervision is consistent with the actual optical observation process. Since this loss constrains the prediction only in the LR measurement domain, the missing HR phase details remain underdetermined. We added a weak high-frequency structural regularization term derived from the HR intensity image,

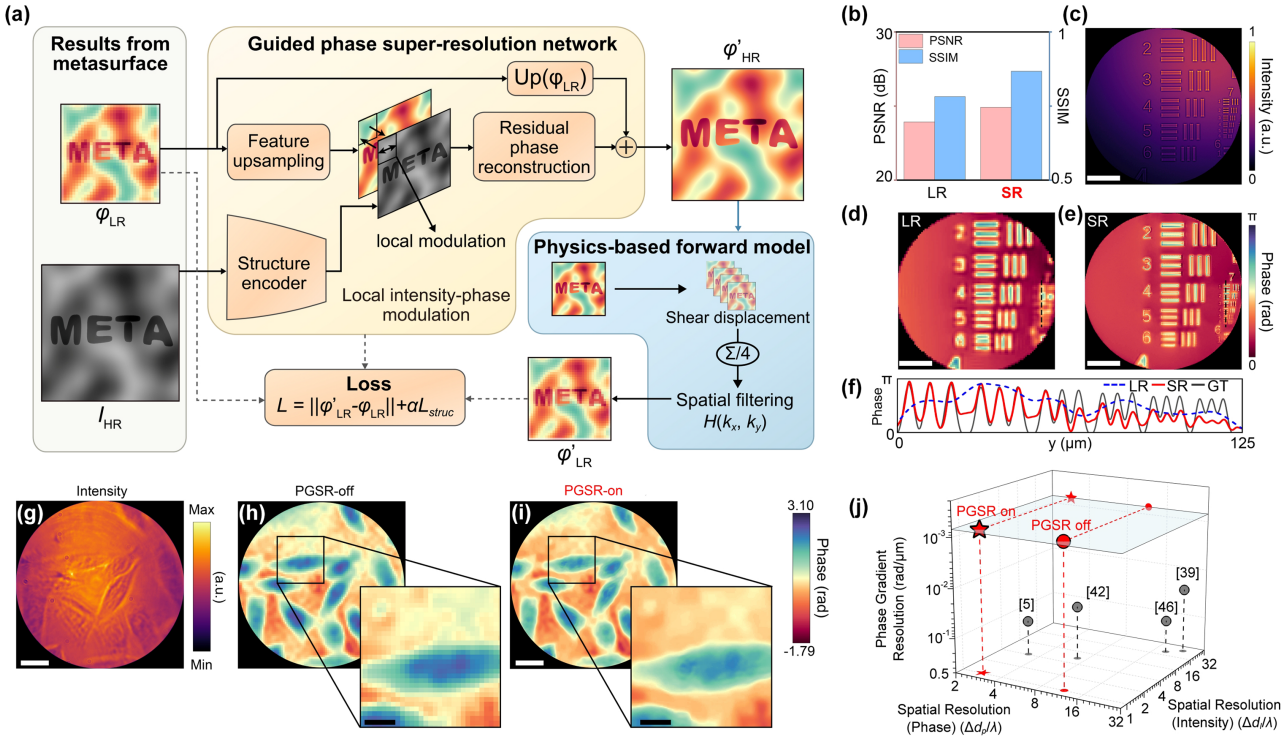


Fig. 4. Deep-learning-enhanced HR imaging for complex-amplitude meta-microscopy. (a) Schematic of the physics-based guided phase super-resolution (PGSR) framework. The network uses the measured HR intensity image as guidance and the LR phase as the baseline to predict a residual HR phase. During self-supervised training, the predicted HR phase is mapped to the LR measurement domain by a differentiable physical forward model, including shear displacement and Fourier-domain filtering, and compared with the measured LR phase to impose physical consistency. (b) Quantitative validation on a public QPI cell dataset [45], demonstrating the enhancement in PSNR and structural similarity index (SSIM) from the LR baseline to the super-resolved (SR) output. (c)–(e) Simulated intensity (c), PGSR-off (LR) phase (d), and PGSR-on SR phase (e) of a USAF 1951 resolution target. (f) Cross-sectional phase profiles along the dashed lines in (d) and (e) (Group 7, Elements 1–6), compared with the ground truth (GT). (g)–(i) Experimental demonstration on living cancer cells. The captured HR intensity (g) is used to guide the enhancement of the raw interferometric phase [(h), PGSR-off], yielding the SR phase [(i), PGSR-on]. Insets show magnified views of the boxed regions. (j) A comparison and summary of the spatial resolution and phase gradient sensitivity in imaging reported in typical literatures and our scheme, demonstrating enhanced performance in resolution metrics [5,39,42,46]. Scale bars: 50 μm in (c)–(e); 10 μm in (g)–(i); 5 μm in magnified insets.

$L_{\text{total}} = L_{\text{phys}} + \alpha L_{\text{struc}}$. This term guides the localization of high-frequency phase details using intensity-derived structural cues, without forcing the phase values to follow the intensity values. The detailed formulation and supporting frequency-dependent correlation analysis are given in Supplement 1, Section S5. For HR phase synthesis, the self-supervised PGSR optimization is performed for 1500 iterations and requires approximately 104 s per image (96 × 96 input, 384 × 384 output). The reconstruction time can decrease to 29 s for a smaller image (32 × 32 input, 128 × 128 output).

For phase-type objects, the intensity channel can still capture an image resulting from the weak scattering effect after light propagation. For example, the intensity image contains no object-dependent absorptive contrast for a phase-only USAF 1951 resolution target with uniform amplitude and binary phase $(0/\pi)$, and the intensity variations arise solely from optical propagation. As shown in Figs. 4(c)–4(e), the network can reconstruct sharp phase boundaries from the 4× degraded LR phase input, and the super-resolution (SR) reconstruction is consistent with the ground-truth (GT) image. This confirms that the model utilizes the LR phase information to recover genuine phase structures enhanced by the HR intensity information. For weakly scattering/absorptive objects such as biological tissue, the meta-microscopy can capture both HR intensity images and initial LR phase images. We evaluated our model on an independent, publicly available Fourier ptychographic microscopy (FPM) dataset [45]. FPM provides a rigorous and independently reconstructed HR phase GT. As shown in Fig. 4(b), our network can recover the HR phase morphology, yielding consistent quantitative improvements over the LR inputs (an increase of ∼0.98 dB in PSNR and ∼0.0844 in SSIM; see more comparison in Fig. S9 in Supplement 1).

We also applied the complex-amplitude meta-microscopy to image label-free live human hepatoma cells (HepG-2). As shown in Fig. S20, Supplement 1, the system employs a paired-objective configuration to project a conjugate real image of the sample onto the operating plane of the metasurface. The metasurface then modulates this incident wavefront to perform both direct intensity imaging and shearing interferometry. The HR intensity image and the interferogram were sequentially captured by rotating the polarizer orientation (which could also be acquired simultaneously using a polarization camera). Figure 4(g) displays the captured HR intensity, while the phase directly reconstructed from the interferogram is shown in Fig. 4(h). By integrating these two channels through PGSR, the phase details are significantly enhanced [Fig. 4(i)]. It should be noted that for objects with strong absorption, this algorithm could be further refined by incorporating prior

absorptive information to distinguish phase contrast from intensity distributions. However, the phase image with the network in Fig. 4(i) still cannot clearly resolve fine structures because the original phase image in Fig. 4(h) is blurred, although the resolution has been increased by four times. To evaluate the recovered effects, we compared the results among the GT, LR, and SR phase images based on the publicly available FPM dataset [45], as shown in the insets of Fig. S10 of Supplement 1. The fine subcellular structures can be recovered by combining the HR intensity image and the LR phase image.

To date, simultaneously enhancing spatial intensity resolution, spatial phase resolution, and phase gradient resolution remains elusive. As shown in Fig. 4(j), compared with existing imaging techniques based on metasurfaces [5,39,42,46], our strategy reaches the state-of-the-art level in phase gradient resolution and spatial resolution, resulting from the balance among the operating NA, interference fringes, two-channel multiplexing, and the neural network. A more comprehensive summary of the reported metrics for related metasurface-based imaging techniques is provided in Supplement 1, Section S12 [47–52]. Although the spatial phase resolution is still limited by the spatial bandwidth, it can be significantly enhanced toward non-interferometric techniques when empowered by the neural network.

D. Dynamic Monitoring of SU-8 Photoresist during UV Exposure

The proposed strategy can be feasibly applied in various scenarios owing to the compact size of the pluggable metasurface. As an example, for material characterization, we measured the dynamic variation of refractive indices during UV exposure to an SU-8 photoresist film. SU-8 is an i-line (exposure at 365 nm) photoresist extensively utilized in semiconductor fabrication, microelectromechanical systems (MEMS), and microfluidic devices. During photolithography, chemical reactions occur in exposed regions, yet the associated refractive index variation is tiny. As a result, direct optical observation of the dynamic exposure process using conventional methods is challenging.

To capture the dynamic material change during the exposure process of the transparent SU-8 photoresist film, we employed an experimental setup combining photomask projection and imaging with the proposed metasurface [Fig. 5(a)]. A common achromatic objective (10×) was used to project the mask pattern onto the SU-8 film (10 μm thickness on a glass substrate, positioned at the mask's optically conjugate plane under 365 nm LED illumination), and to collect the transmitted detection light from a continuous-wave laser operating at 750 nm. The detection light was then reflected by a dichroic mirror toward the metasurface, generating shearing interference. Subsequently, the interference pattern was magnified by a 20× objective lens and captured with a CMOS camera. From the reconstructed phase, the two-dimensional refractive index change $\Delta n(x, y)$ across the observation region was calculated using the formula $\Delta n(x, y) = \varphi(x, y)/(hk_0)$, where k_0 is the wave vector of the detection light in vacuum, and h is the thickness of the SU-8 film. The mask employed in this experiment is Group 2, Element 3 of the USAF-1951 resolution test chart, with a magnification of ∼0.12 in the projection system. Interferogram acquisition was performed since $t = 0$ s, and the 365 nm UV exposure commenced at $t = 60$ s. The interferogram was acquired with a 150 ms exposure time, and the offline phase reconstruction requires ∼60 s per frame on a CPU (Intel Xeon Gold 6246R) or ∼5 s per frame on a GPU (NVIDIA GeForce RTX 3090). Figure 5(b) depicts the time-dependent refractive index changes at three points p_1, p_2, and

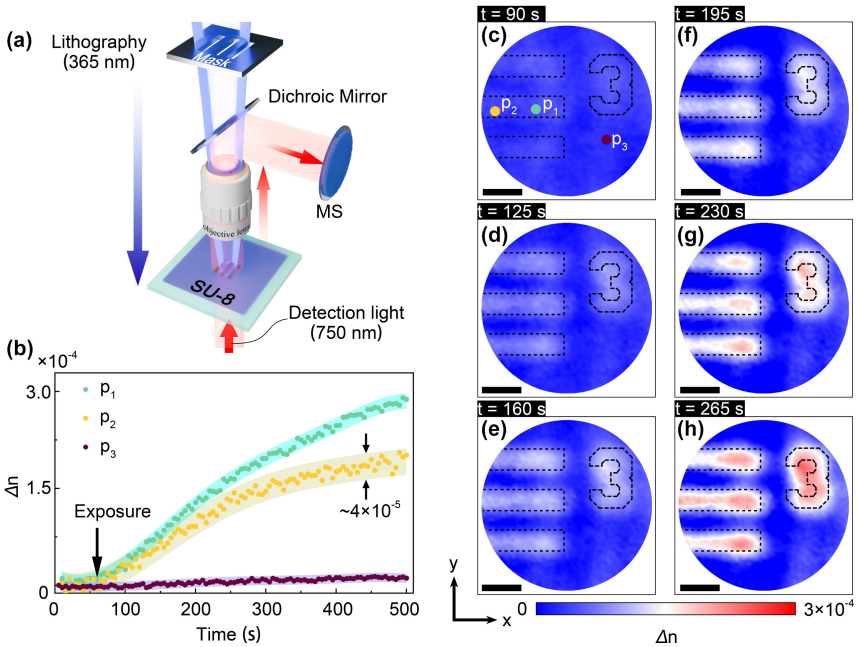


Fig. 5. Quantitative imaging of the dynamic UV exposure process in an SU-8 photoresist film. (a) Schematic of the UV lithography and optical setup based on the proposed pluggable metasurfaces. 365 nm UV light propagates through a photomask and an objective lens, projecting the mask pattern onto the SU-8 photoresist. 750 nm imaging light enters from below and images the SU-8 photoresist by the objective lens and the metasurface to acquire both complex-amplitude distributions. (b) Relative refractive index evolution at points p_1, p_2, and p_3 in (c) over 500 s. UV exposure occurs at 60 s, with points p_1 and p_2 located within the exposed regions and p_3 located in the unexposed region. (c)–(h) Temporal evolution of the relative refractive index (Δn) distribution of the SU-8 film at a 35 s interval. The black dashed line indicates the exposure region governed by the image of the photomask. Scale bar: 15 μm.

p_3 indicated in Fig. 5(c). The spatial distributions of $\Delta n(x, y)$ at various time points are shown in Figs. 5(c)–5(h), where the black dashed boxes denote the ideal exposure region. It is evident that the refractive indices in the exposure region change with the exposure time, which corresponds to the conversion of the photoacid generators (PAGs) in SU-8 to photoacid ($HSbF_6$) under UV exposure. Note that the non-uniformity observed in the exposed region arises from the scattering of exposure light within the SU-8 film and diffusion of the generated photoacid, which is challenging to observe using conventional methods. Besides, as the exposure progresses, the spatial extent of the chemical reaction becomes larger and larger. These results demonstrate that the proposed scheme can clearly resolve such non-uniformity and the material change with the refractive index resolution reaching $\sim 4 \times 10^{-5}$.

3. DISCUSSION

In summary, we propose and experimentally demonstrate HR complex-field meta-microscopy with a compact and pluggable metasurface. A self-supervised SR neural network is designed to enhance phase images by leveraging intensity images as a guide, thereby achieving high spatial and phase-gradient resolution of samples such as label-free cancer cells. We also demonstrate two-dimensional dynamic monitoring of the photoresist exposure process, realizing an ultrahigh refractive-index resolution reaching $\sim 4 \times 10^{-5}$. Taking advantage of polarization-based focusing-interferometry multiplexing and the self-supervised PGSR neural network, our approach enhances the resolution for complex-amplitude imaging compared with existing imaging techniques. Compared with conventional QLSI, our design significantly enhances the diffraction efficiency, eliminates higher-order diffraction, and increases the sampling density owing to the sub-wavelength resonance nature of the nanostructures (Supplement 1, Section S11). The metasurface design also enables the suppression of crosstalk between x- and y-polarization channels, and offers a possibility for other customized phase gradients along multiple directions for noise reduction (Supplement 1, Section S10) [53,54]. Although the zero-order spectrum of the y-polarized interferogram also includes the intensity distribution information, the existence of an x-polarized channel containing an independent intensity image is necessary. That is because the extraction from the zero-order spectrum requires low-pass filtering, which inherently restricts the spatial resolution to the interference fringe period ($p = 6.08\ \mu m$) and introduces potential spectral aliasing with the ± 1st diffraction orders (see the comparison in Fig. S19 in Supplement 1). On the other hand, the HR intensity image in the x-polarized channel enables SR of the LR phase image using the proposed self-supervised neural network.

It should be noted that the strategy using the HR intensity image to super-resolve the LR phase image is based on the assumption that the intensity and phase exhibit a certain degree of structural correlation (more details in Fig. S9 and corresponding discussion in Supplement 1, Section S5), which is valid for biological and weak scattering/absorptive objects. For objects with strong absorption, the algorithm should be further enhanced by incorporating more *a priori* absorptive information and pre-training with ground-truth data to distinguish the phase contrast from the intensity distribution and learn the correlation. More generally, physical, statistical, and network-structural priors, such as forward-model consistency, spatial- and Fourier-domain regularization, and untrained network architectures, could further constrain the recovery of underdetermined high-frequency phase components [55,56]. The spatial complex-amplitude resolution can be further improved by increasing the operating NA with a larger size of the metalens and increasing the shearing momenta to yield a more significant modulation of the fringe period. More analysis about the spatial resolution can be found in Supplement 1, Section S3. The proposed metasurface retrieves the intensity and phase from two separate polarization channels. For applications requiring dual-polarization complex-amplitude imaging such as birefringent media, one could simply integrate the metasurface with a waveplate to switch the polarization. Our work should be of outstanding practical utility in scenarios requiring both compact and HR complex-amplitude imaging. Important examples of such applications in biomedicine include the resolution of subtle tissues and structures in biological tomography and in endoscopes [57]. Quantitative characterization of aberrations in other imaging systems [58] can also be achieved using the proposed method. We also envision that the proposed metasurface can be integrated with a polarized CMOS camera [59] to simultaneously record the two orthogonal polarization channels, avoiding the delay associated with sequential polarization switching. This integration could enable an ultra-compact single-shot complex-amplitude imaging device with high spatial resolution and phase sensitivity. Metaoptics with more complex real-space and k-space responses could also be realized by extended modes [60] and inverse design [61] for more complex multidimensional imaging and detection. Our approach paves the way for high-performance and compact multidimensional imaging applicable to label-free subcellular biological detection, adaptive sensing, quantitative metrology, and micro- and nano-manufacturing, offering new possibilities for the development of next-generation integrated and intelligent imaging systems.

4. MATERIALS AND METHODS

Sample fabrication. The fabrication of the proposed metasurface started with acetone/isopropyl alcohol/deionized water cleaning of a slide glass to promote adhesion between the a-Si:H film and the glass substrate. Then a 500 nm thick a-Si:H film was deposited onto the substrate via plasma-enhanced chemical vapor deposition (Plasmalab 100 from Oxford). After spin coating of an electron beam resist (ZEP520A from Zeon Chemicals), a thin layer of e-spacer 300Z (Showa Denko) was coated to avoid charging during subsequent electron beam exposure. The metasurface pattern was then formed using an electron beam writer (Raith150) and development in ZED-N50. Next, a 60 nm thick Al layer was deposited by e-beam evaporation (Temescal BJD-2000), followed by a lift-off process by soaking the sample in a resist remover (ZDMAC from Zeon Co.). The remaining oval-shaped Al pattern array was used as an etch mask to transfer the designed pattern into the a-Si:H film through fluorine-based inductively coupled plasma-reactive ion etching (Oxford Plasmalab System 100). Finally, the residual Al etch mask was removed by an Al wet etchant.

Cell culture. The HepG-2 cells were purchased from the National Collection of Authenticated Cell Cultures (Shanghai, China) and tested negative for mycoplasma contamination. The HepG-2 cells were cultured in RPMI-1640 medium supplemented with 10% (v/v) FBS, 100 units mL^{-1} penicillin, and 100 $\mu g\ mL^{-1}$ streptomycin in a humidified atmosphere containing 5% CO_2 at 37°C.

Funding. National Key Research and Development Program of China (2021YFA1400601, 2024YFA1409903); National Natural Science Foundation of China (12192253, 11274239, 12274237, 12634012, 12474331, W2441005, U22A20258).

Acknowledgment. Support from the ACT node of the Australian National Fabrication Facility in the form of nanofabrication of the metasurfaces is gratefully acknowledged. Q.L., W.L., H.C., and S.C. initiated the idea. Q.L., W.L., and Y.L. performed the theoretical analysis, numerical simulations, and experiments. D.C. fabricated the samples. Qiang L. cultured the cells. Q.L., W.L., Z.L., Y.L., H.C., and S.C. prepared the paper. S.C. supervised the project. All authors participated in discussions and reviewed the paper.

Disclosures. The authors declare no conflicts of interest.

Data availability. Data underlying the results presented in this paper are not publicly available at this time but may be obtained from the authors upon reasonable request.

Supplemental document. See Supplement 1 for supporting content.

REFERENCES

1. G. R. Fowles, *Introduction to Modern Optics*, 2nd ed. (Dover, 1989).
2. P. C. Chaumet, P. Bon, G. Maire, *et al.*, "Quantitative phase microscopies: accuracy comparison," Light Sci. Appl. **13**, 288 (2024).
3. S. G. Demos and R. R. Alfano, "Optical polarization imaging," Appl. Opt. **36**, 150–155 (1997).
4. Y. Garini, I. T. Young, and G. McNamara, "Spectral imaging: principles and applications," Cytometry A **69A**, 735–747 (2006).
5. H. Kwon, E. Arbabi, S. M. Kamali, *et al.*, "Single-shot quantitative phase gradient microscopy using a system of multifunctional metasurfaces," Nat. Photonics **14**, 109–114 (2020).
6. L. Wesemann, J. Rickett, J. Song, *et al.*, "Nanophotonics enhanced coverslip for phase imaging in biology," Light Sci. Appl. **10**, 98 (2021).
7. Q. Song, A. Baroni, R. Sawant, *et al.*, "Ptychography retrieval of fully polarized holograms from geometric-phase metasurfaces," Nat. Commun. **11**, 2651 (2020).
8. J. Zhou, Y. Jin, L. Lu, *et al.*, "Deep learning-enabled pixel-super-resolved quantitative phase microscopy from single-shot aliased intensity measurement," Laser Photonics Rev. **18**, 2300488 (2024).
9. M. K. Kim, "Digital holographic microscopy," in *Digital Holographic Microscopy: Principles, Techniques, and Applications*, M. K. Kim, ed. (Springer, 2011), pp. 149–190.
10. P. Langehanenberg, B. Kemper, D. Dirksen, *et al.*, "Autofocusing in digital holographic phase contrast microscopy on pure phase objects for live cell imaging," Appl. Opt. **47**, D176–D182 (2008).
11. F. Zernike, "How I discovered phase contrast," Science **121**, 345–349 (1955).
12. S. Fürhapter, A. Jesacher, S. Bernet, *et al.*, "Spiral phase contrast imaging in microscopy," Opt. Express **13**, 689–694 (2005).
13. Y. Guo, Y. Hao, S. Wan, *et al.*, "Direct observation of atmospheric turbulence with a video-rate wide-field wavefront sensor," Nat. Photonics **18**, 935–943 (2024).
14. C. Zheng, W. Wang, Y. Ji, *et al.*, "High-space–bandwidth product characterization of metalenses by information fusion of multi-angle illumination," Optica **12**, 374–383 (2025).
15. G. Baffou, "Wavefront microscopy using quadriwave lateral shearing interferometry: from bioimaging to nanophotonics," ACS Photonics **10**, 322–339 (2023).
16. X. Han, T. Wang, X. Zhang, *et al.*, "Fast and direct calibration for high numerical aperture quadriwave lateral shearing interferometry using geometry model with higher-order Taylor expansion," Appl. Opt. **63**, 6073–6085 (2024).
17. G. Zheng, C. Shen, S. Jiang, *et al.*, "Concept, implementations and applications of Fourier ptychography," Nat. Rev. Phys. **3**, 207–223 (2021).
18. Y. Shu, J. Sun, J. Lyu, *et al.*, "Adaptive optical quantitative phase imaging based on annular illumination Fourier ptychographic microscopy," PhotoniX **3**, 24 (2022).
19. C. Zuo, J. Li, J. Sun, *et al.*, "Transport of intensity equation: a tutorial," Opt. Lasers Eng. **135**, 106187 (2020).
20. J. Zhang, Q. Chen, J. Sun, *et al.*, "On a universal solution to the transport-of-intensity equation," Opt. Lett. **45**, 3649–3652 (2020).
21. K. Wang, L. Song, C. Wang, *et al.*, "On the use of deep learning for phase recovery," Light Sci. Appl. **13**, 4 (2024).
22. G. Zhang, T. Guan, Z. Shen, *et al.*, "Fast phase retrieval in off-axis digital holographic microscopy through deep learning," Opt. Express **26**, 19388–19405 (2018).
23. F. Aieta, M. A. Kats, P. Genevet, *et al.*, "Multiwavelength achromatic metasurfaces by dispersive phase compensation," Science **347**, 1342–1345 (2015).
24. W. T. Chen, A. Y. Zhu, and F. Capasso, "Flat optics with dispersion-engineered metasurfaces," Nat. Rev. Mater. **5**, 604–620 (2020).
25. M. Khorasaninejad, W. T. Chen, R. C. Devlin, *et al.*, "Metalenses at visible wavelengths: diffraction-limited focusing and subwavelength resolution imaging," Science **352**, 1190–1194 (2016).
26. R. J. Lin, V.-C. Su, S. Wang, *et al.*, "Achromatic metalens array for full-colour light-field imaging," Nat. Nanotechnol. **14**, 227–231 (2019).
27. Z. Dong, L. Jin, S. D. Rezaei, *et al.*, "Schrödinger's red pixel by quasi-bound-states-in-the-continuum," Sci. Adv. **8**, eabm4512 (2022).
28. E. Choi, G. Kim, J. Yun, *et al.*, "360° structured light with learned metasurfaces," Nat. Photonics **18**, 848–855 (2024).
29. A. Arbabi, Y. Horie, M. Bagheri, *et al.*, "Dielectric metasurfaces for complete control of phase and polarization with subwavelength spatial resolution and high transmission," Nat. Nanotechnol. **10**, 937–943 (2015).
30. J. P. B. Mueller, N. A. Rubin, R. C. Devlin, *et al.*, "Metasurface polarization optics: independent phase control of arbitrary orthogonal states of polarization," Phys. Rev. Lett. **118**, 113901 (2017).
31. Y.-J. Gao, X. Xiong, Z. Wang, *et al.*, "Simultaneous generation of arbitrary assembly of polarization states with geometrical-scaling-induced phase modulation," Phys. Rev. X **10**, 031035 (2020).
32. A. H. Dorrah and F. Capasso, "Tunable structured light with flat optics," Science **376**, eabi6860 (2022).
33. A. Overvig and A. Alù, "Diffractive nonlocal metasurfaces," Laser Photonics Rev. **16**, 2100633 (2022).
34. W. Liu, D. Ma, Z. Li, *et al.*, "Aberration-corrected three-dimensional positioning with a single-shot metalens array," Optica **7**, 1706–1713 (2020).
35. W. T. Chen, A. Y. Zhu, V. Sanjeev, *et al.*, "A broadband achromatic metalens for focusing and imaging in the visible," Nat. Nanotechnol. **13**, 220–226 (2018).
36. F. Zhang, G. Han, Y. Tian, *et al.*, "Monolithic expandable-FOV metalens enabled by radially gradient-tilted meta-atoms," Opt. Lasers Eng. **200**, 109615 (2026).
37. F. Yesilkoy, E. R. Arvelo, Y. Jahani, *et al.*, "Ultrasensitive hyperspectral imaging and biodetection enabled by dielectric metasurfaces," Nat. Photonics **13**, 390–396 (2019).
38. J. Xiong, X. Cai, K. Cui, *et al.*, "Dynamic brain spectrum acquired by a real-time ultraspectral imaging chip with reconfigurable metasurfaces," Optica **9**, 461–468 (2022).
39. G.-H. Go, D.-G. Lee, J. Oh, *et al.*, "Meta Shack–Hartmann wavefront sensor with large sampling density and large angular field of view: phase imaging of complex objects," Light Sci. Appl. **13**, 187 (2024).
40. Q. Min, J. Trapp, T. Fang, *et al.*, "Varifocal metalens for compact and accurate quantitative phase imaging," ACS Photonics **11**, 2797–2804 (2024).
41. Y. Xue, J. Min, L. Yang, *et al.*, "High-resolution quantitative phase camera utilizing a polarization-modulated diffractive optical element," Optica **12**, 1820–1829 (2025).
42. L. Li, S. Wang, F. Zhao, *et al.*, "Single-shot deterministic complex amplitude imaging with a single-layer metalens," Sci. Adv. **10**, eadl0501 (2024).
43. H. R. Sheikh, M. F. Sabir, and A. C. Bovik, "A statistical evaluation of recent full reference image quality assessment algorithms," IEEE Trans. Image Process. **15**, 3440–3451 (2006).
44. M. A. Herráez, D. R. Burton, M. J. Lalor, *et al.*, "Fast two-dimensional phase-unwrapping algorithm based on sorting by reliability following a noncontinuous path," Appl. Opt. **41**, 7437–7444 (2002).
45. L. Tian, X. Li, K. Ramchandran, *et al.*, "Multiplexed coded illumination for Fourier Ptychography with an LED array microscope," Biomed. Opt. Express **5**, 2376–2389 (2014).
46. S. Yi, J. Xiang, M. Zhou, *et al.*, "Angle-based wavefront sensing enabled by the near fields of flat optics," Nat. Commun. **12**, 6002 (2021).
47. L. Li, W. Jia, C. Jin, *et al.*, "Single-shot wavefront sensing with nonlocal thin film optical filters," Laser Photonics Rev. **17**, 2300426 (2023).
48. Q. Wu, J. Zhou, X. Chen, *et al.*, "Single-shot quantitative amplitude and phase imaging based on a pair of all-dielectric metasurfaces," Optica **10**, 619–625 (2023).

49. A. Ji, J.-H. Song, Q. Li, *et al.*, "Quantitative phase contrast imaging with a nonlocal angle-selective metasurface," Nat. Commun. **13**, 7848 (2022).
50. A. Shanker, J. E. Fröch, S. Mukherjee, *et al.*, "Quantitative phase imaging endoscopy with a metalens," Light Sci. Appl. **13**, 305 (2024).
51. J. Wang, J. Sun, J. Li, *et al.*, "Plan meta-objective for sub-micron quantitative phase imaging," Light Sci. Appl. **15**, 71 (2026).
52. G.-Y. Lee, C. Kim, M. Gopakumar, *et al.*, "Neural phase microscopy with metasurface optics for real-time and nanoscale quantitative phase imaging," Nat. Commun. **17**, 1411 (2026).
53. R. Legarda-Sáenz and A. Espinosa-Romero, "Wavefront reconstruction using multiple directional derivatives and Fourier transform," Opt. Eng. **50**, 040501 (2011).
54. H. Zhong, Y. Li, K. Liu, *et al.*, "Zonal wavefront reconstruction with multidirectional difference wavefronts for multilateral shearing interferometers," Appl. Opt. **64**, 5149–5157 (2025).
55. Y. Gao, L. Cao, and D. P. Tsai, "Single-shot, reference-less computational wavefront sensing for complex optical fields," Light Sci. Appl. **15**, 174 (2026).
56. F. Wang, Y. Bian, H. Wang, *et al.*, "Phase imaging with an untrained neural network," Light Sci. Appl. **9**, 77 (2020).
57. Z. Huang and L. Cao, "Quantitative phase imaging based on holography: trends and new perspectives," Light Sci. Appl. **13**, 145 (2024).
58. B. Liu, J. Cheng, M. Zhao, *et al.*, "Metalenses phase characterization by multi-distance phase retrieval," Light Sci. Appl. **13**, 182 (2024).
59. J. Zuo, J. Bai, S. Choi, *et al.*, "Chip-integrated metasurface full-Stokes polarimetric imaging sensor," Light Sci. Appl. **12**, 218 (2023).
60. H. Qin, Z. Su, Z. Zhang, *et al.*, "Disorder-assisted real–momentum topological photonic crystal," Nature **639**, 602–608 (2025).
61. Z. Li, R. Pestourie, J.-S. Park, *et al.*, "Inverse design enables large-scale high-performance meta-optics reshaping virtual reality," Nat. Commun. **13**, 2409 (2022).